

Rapid vortex ring bubble transport via bubble-pulsation of constrained underwater spark discharge

Received: 31 December 2024

Accepted: 23 June 2025

Published online: 05 July 2025



Xutong Wang^{1,2,8}, Yantao Feng^{3,8}, Shuran Li^{1,2,4}✉, Hong Cao^{1,2}, Shuo Zhang^{3,5}, Zhen Liu^{3,5}, Yanliang Pei^{6,7}, Weidong Zhu^{1,2,4}, Xiaowen Song^{1,2}, Yinglin Ke^{1,2,4} & Keping Yan^{3,5}

The transport of gas bubbles in liquid environments is essential across applications like microfluidics, drug delivery, and energy systems, but achieving stable, high-speed motion remains a challenge. We present an advanced implementation of submerged spark discharge-driven ring bubble generation by leveraging the dynamic interactions and fluid motion at high velocities and accelerations generated by high initial overpressure, achieving high-circulation bubbles that reach initial velocities of 12 m/s, travel 800 mm, which also can be generated in extreme stroke ratios and minimal space. Key features include self-contained movement, collision resilience, and adaptability across media. Scalable and programmable, this method enables precision in bubble manipulation, paving the way for advanced applications in fluid transport, environmental engineering, and biomedical systems.

Gas bubble transport within liquid environment is crucial for optimizing materials and energy exchange across diverse applications, including drug delivery¹, water electrolysis², microfluidics³, energy storage⁴, wastewater recycling⁵, gas catalysis⁶, and other fields. Furthermore, the performance of bubble transport critically depends on their motion velocity⁷. For instance, increasing bubble velocity can significantly boost the efficiency of boiling heat transfer on a heated surface, and suppress coalescence to 1/10 of its original rate in multiphase systems⁸. To date, existing strategies for manipulating gas bubbles primarily rely on the assistance of optofluidics⁹, buoyancy force¹⁰, or wetting driving force¹¹ from functional material surfaces. These traditional approaches can influence spherical bubble direction or volume, while controlling bubble behavior—specifically motion velocity, translational distance, and stable orientation—remains elusive due to inherent instability and drag-induced deflection underwater. As a breakthrough in 2021, the pre-chaotic behavior of vortex bubbles

was proved to stabilize dynamic non-equilibrium states, resulting in improved efficiency in maintaining bubble stability and dynamic control¹². Compared to spherical bubbles, the internal gas circulation within ring-shaped bubbles facilitates efficient heat exchange and mass transfer, contributing to their impressive persistence and mobility in fluid environments¹³. For example, vortex ring bubble is observed to be necessary for regular filling-to-ejection transition within left ventricle¹⁴.

The practical deployment of vortex rings for material delivery hinges critically on achieving high-speed, long-distance transport and exchange with exceptional stability. This necessitates the generation of vortex rings characterized by substantial circulation. Conventional methods, using impulsive fluid discharge through nozzles or orifices, are inherently limited, with circulation values capped at $\sim 10^3 \text{ cm}^2/\text{s}$ ¹⁵. Consequently, the ring bubble with limited circulation are particularly prone to viscous effects, which diminishes vorticity and progressively

¹State Key Laboratory of Fluid Power and Mechatronic Systems, School of Mechanical Engineering, Zhejiang University, Hangzhou 310027, China. ²Key Laboratory of Advanced Manufacturing Technology of Zhejiang Province, School of Mechanical Engineering, Zhejiang University, Hangzhou 310027, China. ³College of Chemical and Biological Engineering, Zhejiang University, Hangzhou 310028, China. ⁴Donghai Laboratory, Zhoushan 316000, China. ⁵Shanxi-Zheda Institute of Advanced Materials and Chemical Engineering, Taiyuan 030002, China. ⁶Laboratory for Marine Geology, Laoshan Laboratory, Qingdao 266000, China. ⁷Key Laboratory of Marine Geology and Metallogeny, First Institute of Oceanography, Ministry of Natural Resources, Qingdao 266061, China. ⁸These authors contributed equally: Xutong Wang, Yantao Feng. ✉ e-mail: lisr@zju.edu.cn

depletes kinetic energy¹⁶. Moreover, asymmetrical vorticity changes in the vortex ring induce differential movement between the upper and lower vortex cores, resulting in a net displacement of the vortex ring's center, thus restricting the potential applications of the ring-shaped bubble primarily to vertical upward movement. Many recent methodologies are centered on the utilization of compressed air or piston, while the piston-based systems suffer from the production of relatively low-velocity vortex rings and device size limitations. Furthermore, compressed gas methods often lead to turbulent flows with structure piercing, generating multiple rings with azimuthal instability at high circulation, or bubble-entrained trails at low migration velocities (see Supplementary Fig. S1). Ring bubble with high circulation is fundamentally caused by the high velocity and acceleration of the acting fluid¹⁷, underscoring the critical role of dynamic fluid properties in achieving good vortex transport performance. However, traditional drivers often fail to deliver sufficient exhaust velocity, leading to time-reversible boundary motions that render vortex bubbles ineffective in the Stokes regime¹⁸. Specifically, the linear velocity of the fluid medium in piston or compressed gas methods is limited to 4 m/s. The acceleration achieved by the piston method is only 2.5 m/s²¹⁹, while the compressed gas method can reach up to 22 m/s². Therefore, alternative strategies are required to generate vortex rings with substantially greater circulation over very short timescales.

The cavitation process of underwater discharge affects the flow field in an extremely short time with an extremely fast expansion speed^{20–23}. Under the spatial constraint of a certain mutation cross section, secondary cavitation can be formed^{24–27}, but its energy is relatively low and is unable to form a vortex ring with higher circulation and higher speed. We recognized the potential of unidirectional ring bubble transport under the dual influence of discharge process and fluid dynamics in the presence of irregular boundary conditions. Herein, an isolated and stable ring bubble is generated by adopting a submerged spark discharge in saline water with a rough boundary, and demonstrates characteristics of being self-contained, self-propelling, and notably long-lasting. The high-speed observation and physical mechanism of the submerged sparker induced ring bubble is proposed by taking into account the formation of the primary bubble cavitation and the associated shear effect at the fluid interface. We conduct scaling analysis and numerical simulations, both of which show excellent agreement with the observations. Based on its tens of times higher circulation than piston and compressed gas methods, the vortex ring exhibits remarkable horizontal motion capabilities, achieving a maximum velocity of up to 12 m/s and a translational distance of 800 mm under experimental conditions, with a center displacement of only 8 mm. Moreover, the expansion and subsequent collapse of the initial bubble minimize turbulence effects compared to the severe turbulence associated with compressed gas methods, avoiding vertical instabilities caused by piercing. The method offers a broader range of adjustable stroke ratios than the finite mechanical constraints of pistons, enabling the formation of extremely small vortex rings. A scalable, programmable solution for manipulating gas bubbles is developed, capable of generating ring bubbles within a 1-mm-diameter capillary tube. Further, through the production of highly repeatable vortex rings, we successfully demonstrated the characteristics of these self-stabilizing, high-speed rings. The vortex rings achieved gas transport, particle transport, cross-medium transitions and long-distance linear migration with markedly negligible self-contained gas volume of 0.1 μL . Throughout this process, the ring bubbles exhibited exceptional collision exchange and disturbance resistance capabilities, indicating the potential for advanced, miniaturized and high-capacity bubble transport devices.

Results

Observation of the ring bubble

A microsecond electric pulse vaporizes the liquid surrounding the electrode tip by energizing a coaxial in-pipe electrode positioned

5–10 mm from the pipe's opening. The compression of the incompressible gases inside the subsequent spherical bubble overcomes the high pressures in the liquid around, thereby emitting a shock wave²⁸. The incompressibility of the liquid induces deformation and cavitation along the inner edge of the pipe opening. Subsequently, a secondary ring-shaped bubble forms in an extremely short time and is expelled forward when the output energy exceeds 0.5 J. Remarkably, rather than collapse in several microseconds like the initial bubble, the secondary ring bubble demonstrates rapid, linear transport over considerable distances with initial high circulation, as illustrated in Fig. 1A. The ring bubble in Fig. 1B represents an underwater vortex ring with a vortex core containing only a few nanoliters of gas. The smooth toroidal bubble, when formed, travels quickly apart from the residual primary bubbles.

The submerged copper electrode is encapsulated by a polytetrafluoroethylene layer to generate a high localized breakdown electric field at the electrode tip (Supplementary Fig. S2). The ring bubble emerges ~30 μs following the formation of the primary bubble with a substantial initial velocity. Throughout the migration phase, which spans up to 2000 ms, both the major and minor diameters of the ring bubble exhibit pronounced oscillations initially, followed by a gradual decrease in oscillatory amplitude (Fig. 1C, Fig. 1D and Movie S1). The submerged spark discharge is energized by a homemade pulse power supply (Fig. 1E and Supplementary Fig. S3).

The submerged sparker within a constraint tube acts as a catapult, utilizing accumulated energy to propel the ring bubble at high speed. As shown in Fig. 1F, the primary bubble expands only 30 mm with a leading-edge velocity reaching up to 30 m/s, whereas the resulting ring-shaped bubble demonstrates remarkable transport capabilities, migrating over 800 mm at a stable velocity of 1–4 m/s. The ring bubble achieves significantly greater persistence and translational distance than the primary bubble, while containing only 8% of the primary bubble's volume. Although its peak velocity is lower, the ring bubble maintains a higher average velocity throughout its migration (Fig. 1G).

Formation of submerged sparker and vortex ring

Figure 2A shows the submerged spark discharge can manipulate the changes in the flow field through bubbles and walls. Figure 2B illustrates the submerged spark discharge mechanism, initiating with the formation of a high-temperature, high-pressure bubble, accompanied by intense luminescence (within 0.4–0.9 ms; the spectral characteristics are detailed in Supplementary Fig. S4 and Supplementary Table S2.). The discharge electron temperature range of the constraint tubes is calculated as 10000–11300 K, and the unconstrained tubes is 10000–13000 K^{29–31}. There is a certain correlation between energy and electron temperature. The cylindrical configuration of the primary bubble suppresses the rapid release of pulsed discharge energy. At extremely high temperatures, there will be a certain amount of melting and ablation of the copper electrode tip and microporous erosion caused by cavitation (Supplementary Figs. S5, S6)^{32,33}. The bubble expands rapidly under elevated pressure and continues to expand due to liquid inertia even after its internal pressure equilibrates with the ambient medium³⁴. Subsequently (within 1.2–1.8 ms), opposing pressures arrest the outward momentum, and the top of the bubble flattens and subsequently evolves into a downward-propagating internal jet which persists until it impacts the bottom of the bubble, leading to instability and fragmentation. The pressure variation follows the Rayleigh-Plesset equation (Eq. 1), see Supplementary Fig. S7³⁵.

$$\rho \left(R_g \ddot{R}_g + \frac{3}{2} \dot{R}_g^2 \right) = P_{\text{in}}(t) - P_{\text{out}} - \frac{2\gamma}{R_g} - 4\mu \frac{\dot{R}_g}{R_g} \quad (1)$$

Under spatially constrained conditions, the submerged sparker induces a morphological transition of the bubble from a spherical to a

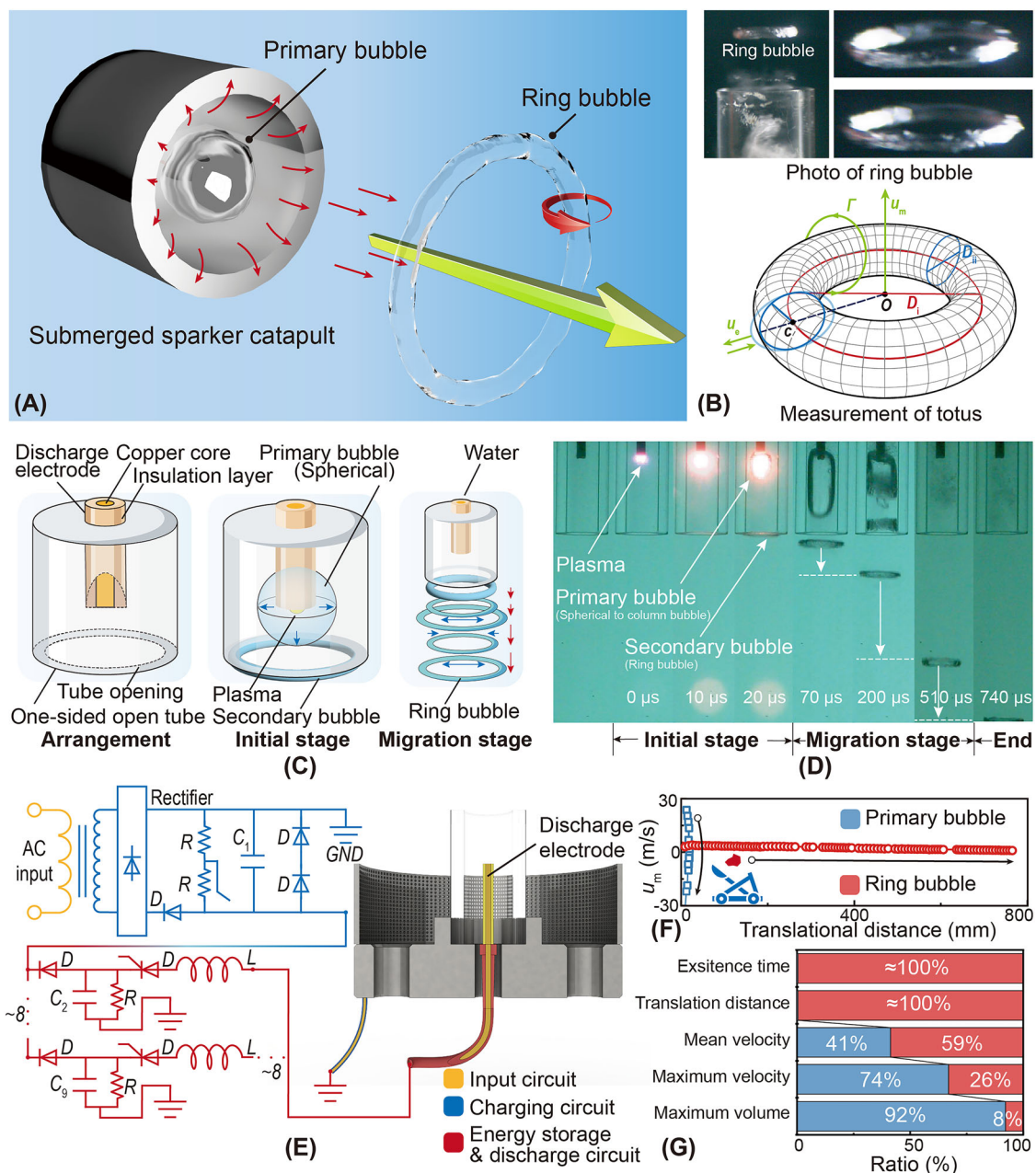


Fig. 1 | Observation of the ring bubble induced by submerged sparker catapult.

A Schematic representation of the submerged sparker catapult producing a primary bubble, which subsequently forms a ring bubble that is propelled forward. The green and red arrow represent unidirectional motion and rotational motion, respectively. **B** Photographs and schematic, showing the measurements of the toroidal structure. Symbols are in Supplementary Table S1. **C** Illustration of the initial arrangement of submerged sparker catapult, the formation of the primary bubble, and the subsequent migration and oscillation of the ring. **D** Sequential high-speed images capturing the temporal evolution from plasma formation to the generation of the primary and ring bubbles at various time intervals (with 10000 fps frame rate at $E_{out} = 1.4$ J, $t = 0$ μ s for the moment right when the underwater spark discharge initiates). **E** Schematic of the pulse power supply used to energize

the submerged sparker, showing the input, charging, and energy storage circuits. The right side of the figure shows a cross-sectional view of the submerged sparker device. The central orange component represents the discharge electrode ($\phi_e = 0.7$ mm) and the attached high-voltage cable. The transparent hard interface surrounding it is a quartz tube ($\phi_{tube} = 10$ mm, $T_{tube} = 2$ mm, distance from electrode to tube opening = 12 mm). The outermost mesh serves as the grounding electrode. **F** Comparison of the migration velocities between the primary and ring bubbles as a function of translational distance, highlighting the enhanced stability and persistence of the ring bubble. **G** Comparative metrics of the primary and ring bubbles. The data represents the normalized proportion of individual bubbles and rings, demonstrating the superior endurance and distance coverage of the ring bubble relative to the primary bubble. Source data is provided as a Source Data file.

cylindrical configuration, thereby generating a flow field that sustains the initial vortex ring and extends the lifespan (0.3–0.8 ms) of the primary bubble in Fig. 2C, and see Supplementary Fig. S7 for a comparison of bubbles with and without constraint. The cylindrical configuration of the primary bubble suppresses the rapid release of pulsed discharge energy, thereby moderating and prolonging the pulse current, as demonstrated in Fig. 2D. When the primary bubble contacts

and subsequently separates from the vortex ring bubble (stages 3–4), the output voltage drops precipitously to zero, establishing the necessary conditions for the prompt initiation of the subsequent discharge.

When the fluid driven by bubbles flows in the tube, due to the existence of the boundary layer, the fluid molecules near the inner wall move slowly, while the fluid molecules far from the wall move quickly

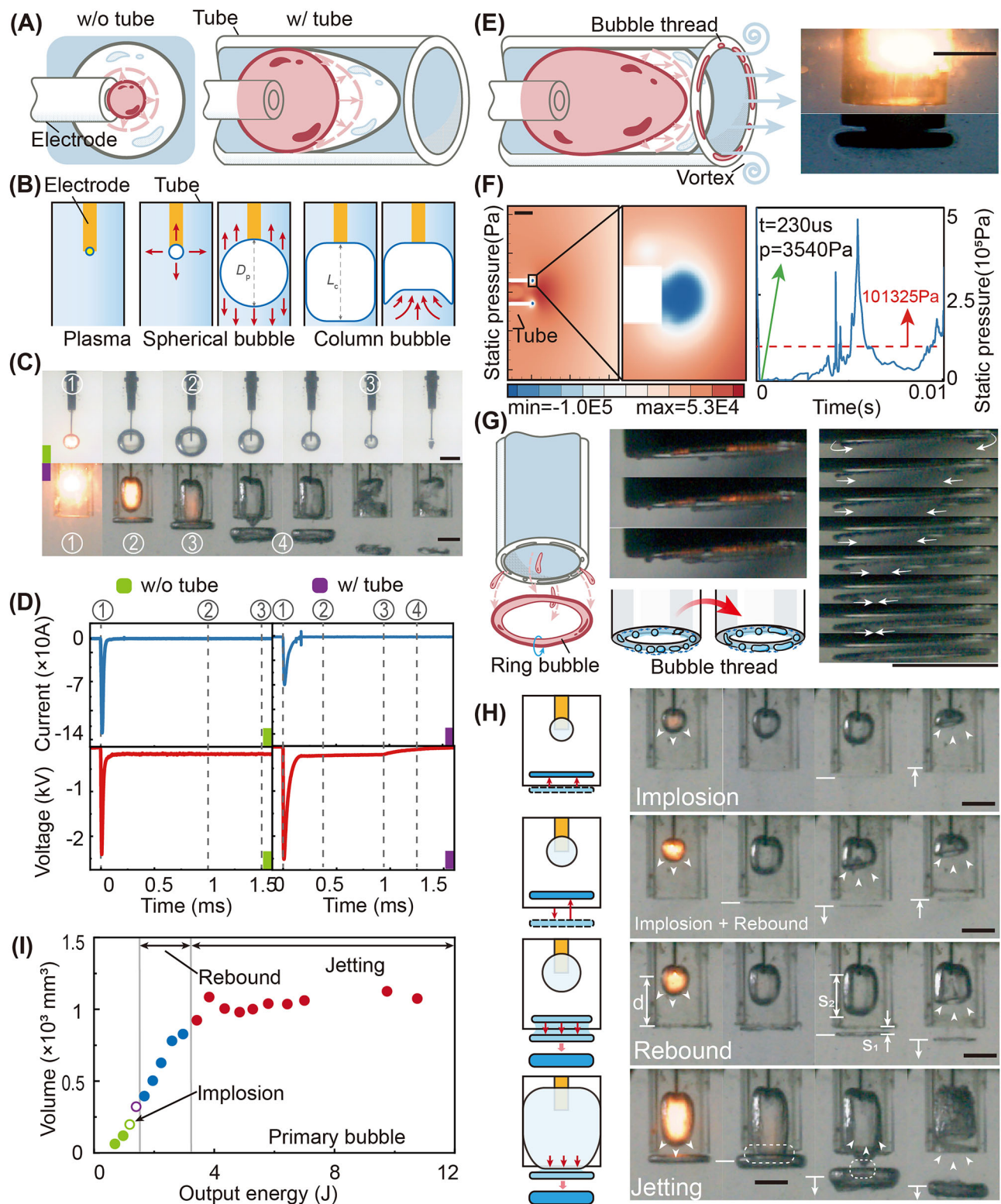


(Fig. 2E), thus forming a certain velocity gradient to reduce the pressure at the nozzle. Compared with other methods, the expansion of the primary bubble can produce greater fluid velocity and acceleration, and form a large velocity difference with the external fluid at an extremely high speed at the nozzle, causing a huge pressure drop. In addition, since the shock wave generated by the initial explosion is spherical and hits the water body quickly, negative pressure effect will be generated afterwards (Supplementary Fig. S8), and the front end of the bubble is not a plane, which will further increase the velocity gradient along the

radial direction of the pipeline, so the nozzle pressure is further reduced, and finally low pressure is quickly generated at the nozzle and cavitation occurs (Fig. 2F and Supplementary Figs. S9, S10)³⁶. The nozzle velocity difference generated by the jet will also form a relative flow of the fluid. The schlieren experiment in Fig. 2E captured this enhanced velocity gradient, causing the jet to be sucked into a vortex flow field at the nozzle outlet. Since the rotating flow of the liquid in the vortex flow field will produce a low-pressure area inside it, and the pressure drop of the rotating fluid is strong, compared with other cavitation phenomena,

Fig. 2 | Submerged spark discharge process and formation of vortex ring bubble. **A** Submerged discharge changes the electrode environment constraints, changes the bubble development morphology and trend, ultimately controls the local flow field. **B** Schematic of the formation and evolution of the primary bubble, transitioning from a spherical to a cylindrical configuration under the influence of the tube boundary. **C** Sequential high-speed images showing the evolution of the primary bubble and the formation of the vortex ring bubble under or without tube. **D** Voltage and current waveforms during the discharge process, illustrating the impact of the boundary constraint on electrical characteristics. **E** The enhanced boundary layer velocity gradient formed by the local flow field in tube and vortex formed by the flow field entrainment at the nozzle. The right picture shows the direction of fluid flow at the nozzle captured by high-speed camera and schlieren photography. **F** The velocity gradient at the nozzle causes low pressure at the nozzle, which is lower than the cavitation pressure, causing bubbles to form at the

nozzle, and the cavitation range becomes larger. At the same time, the vorticity gradually increases. **G** Schematic depicting the formation of bubble threads and their connection to form a ring bubble under the influence of vortex flow. High-speed camera images capturing the rapid formation of a complete ring-shaped bubble from cavitation bubble threads, with arrows indicating the direction of connection. **H** Representative high-speed images of the four primary bubble modes, highlighting the differences in their collapse and interactions leading to vortex ring bubble formation. In implosion, the primary bubble undergoes rapid collapse, immediately drawing the vortex ring bubble into the tube. In implosion + rebound, the ring bubble traverses a short distance before being absorbed. **I** Volume of the primary bubble as a function of output energy. The discharge current and voltage of these four modes increase sequentially, while the half-pulse width gradually decreases. Scale bars, 10 mm. Source data are provided as a Source Data file.

cavitation is easier to occur and maintain in the core area of the vortex³⁶. The vortex generated by the high-speed jet rotates fast, so that the core area of the vortex quickly forms a sufficiently low negative pressure, so the cavitation can occur quickly and maintain its shape under the combination of the two. Figure 2G and Supplementary Fig. S11 illustrates the rapid connection of these bubble threads under high pressure and expansion. The overall initial cavitation gas has a high pressure and expands outward to form an initial gas vortex ring, culminating in the formation of a complete ring bubble rapidly within 0.3–0.35 microseconds (Movie S2). When the confinement tube is narrow, the vortex ring forms a few millimeters away from the tube's opening (Movie S3). The gas ring will migrate to the lowest pressure area in the vortex, that is, the center of the vortex and merge together³⁷, eventually the continuous movement of the vortex will drive the vortex ring bubble to move.

Submerged discharges exhibit four modes: implosion, implosion + rebound, rebound, and jetting (Fig. 2H). Bubble expansion, faster than ring migration, injects energy into the ring. In jetting, if the bubble's travel distance s_2 exceeds both the ring's migration and the electrode-nozzle gap ($s_1 + d$), dynamic interaction between primary bubble and ring bubble drives gas exchange that enhances ring volume and stability.

Figure 2I and Supplementary Fig. S12 demonstrates that the implosion + rebound mode (purple hollow circle) occurs only at 1.4 J (a critical threshold). From 1.5–3 J, rebound dominates and vortex-ring volume grows with energy; above 3 J, jetting takes over, bubble volume stabilizes, and stability enhanced. Both rebound and jetting impart greater initial kinetic energy via rapid, concentrated injection. The existence of a constrained tube widens the discharge pulse versus unconstrained discharges, prolongs the primary bubble, and maintains the growing vorticity flux before pinch off. A sufficiently strong primary bubble spawns a secondary ring inside the tube; although merging with the main vortex would be destabilizing, the high velocity of the main vortex and the contraction flow of the primary bubble will push the secondary ring back into the tube (Movie S4), thus maintaining the stability of the primary ring.

Oscillatory behavior of the ring bubble

The translational dynamics and stability of a ring bubble are fundamentally governed by the interaction between vorticity in the surrounding flow field and forces acting on the bubble. The equilibrium of a ring bubble results from the radial pressure gradient-induced force counterbalanced by competing forces [$\frac{\rho u_{\theta}^2}{R_0} = \frac{\pi}{8} \rho C_D D_i^2 u_{b,r}^2$]. Figure 3A shows that due to the small initial ring size, it will expand and shrink like a bubble. However, due to the high vortex volume, the low cavitation pressure can be maintained for a long time. Therefore, the vortex ring does not break after contraction, but oscillates forward. Figure 3B demonstrates the effect of the equilibrated vortex ring on the nearby fluid. The local velocity distribution of the vortex ring is shown in Supplementary Fig. S13. At elevated circulation values (Γ)

[$\Gamma = \oint_C \mathbf{u} \cdot d\mathbf{r}$], the equilibrium position shifts closer to the vortex core, driven by alterations in the vorticity field. This phenomenon extends beyond the radial force balance, necessitating consideration of modifications in core vorticity³⁸. The findings suggest that higher energy inputs amplify circulation, yielding extending periods of elevated circulation.

Figure 3C compares the mean circulation (Γ_m) of ring bubbles generated by different methods. Gravity-driven and piston-driven methods yield circulations comparable to the rebound + implosion mode, while compressed gas-driven methods achieve circulation levels characteristic of the rebound mode. Clearly, within the lower energy range, the formation and dynamic properties of vortex ring bubbles are closely linked to the tube's bubble diameter and the associated impulsively discharging fluid. When the output energy increases, both the diameter and the period of the primary bubble exhibit nearly linear growth. In the higher energy range, bubble diameter grows above the inner diameter of the tube, but its volume can still be increased along the column. Therefore, it is still possible to cause a change in onset pressure to drive the circulation up. The pressure of compressed air generally falls within 25–75 kPa with durations of 0.2–0.3 seconds¹⁵, comparable to the rebound mode. Notably, maximum circulation stabilizes once the input energy exceeds jetting mode, consistent with the observation that bubbles at high circulation positions near the vortex core are influenced by core vorticity modifications, the onset pressure of the primary bubble approaches stability upon entering the jetting mode, reducing the correlation between the characteristics of vortex ring bubbles and primary bubbles (see Supplementary Fig. S7).

Figure 3D shows that the oscillation decay of the vortex flow field causes the oscillation decay of the circulation. The core radius R_c (R_{c0}), ring radius R (R_0), the radius ratio $\varepsilon = R_c / R$, and Saffman formula for calculating the volume are following Eq. 2³⁹. In an incompressible fluid, the initial decay state⁴⁰ of the circulation conforms to the Hamel-Ossen exponential decay model (Eq. 3), and for a long time it conforms to the decay form of the power function [$\Gamma = a_1 \Gamma_0 t^{b_1}$]. According to the bubble ring Rayleigh-Plesset equation, the circulation affects the frequency and amplitude of the ring oscillation (Eq. 4 and Fig. 3E, F).

$$\Gamma = \frac{4\pi R_c u_m}{\left\{ \varepsilon \left[\ln \frac{8}{\varepsilon} - \frac{1}{2} + \frac{\gamma/R_c}{\rho(\Gamma/2\pi R_c)^2} \right] + O(\varepsilon) \right\}} \quad (2)$$

$$\Gamma = \Gamma_0 \left(1 - \exp \left[\frac{-R_c^2}{4\nu t} \right] \right) \quad (3)$$

$$\rho(R\ddot{R}_c + \dot{R}_c^2) \ln \frac{8R_0}{R_c} - \frac{1}{2} \rho \dot{R}_c^2 = p_v - p_\infty(t) + \frac{1}{2} \rho \left[\frac{\Gamma}{2\pi R_c} \right]^2 + p_{g0} \left(\frac{R_{c0}}{R_c} \right)^{2k_i} - \frac{\gamma}{R_c} \quad (4)$$

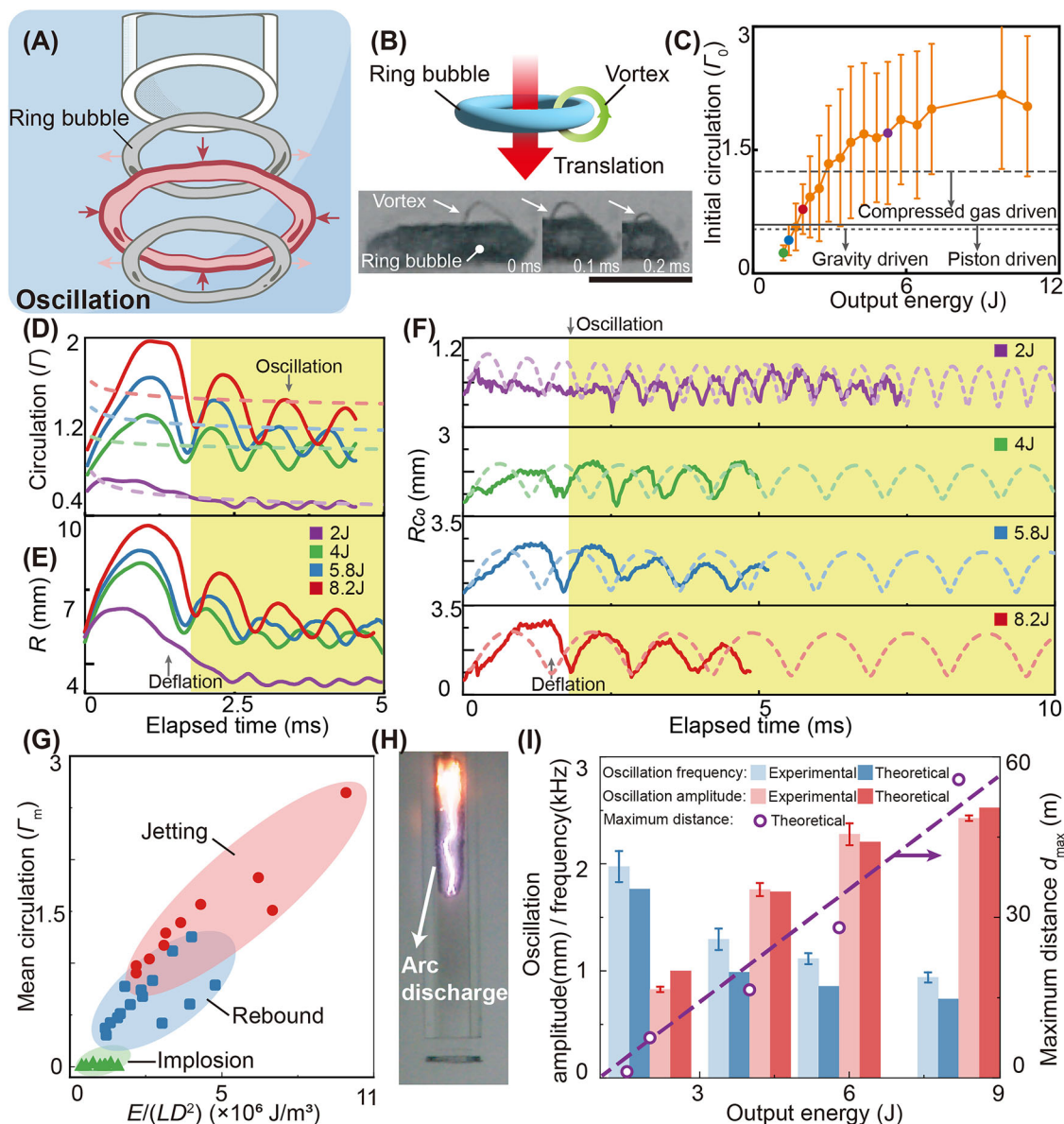


Fig. 3 | Oscillating behavior of bubble ring. **A** Under the action of the initial pressure, the bubble ring expands and contracts, and its radius oscillates repeatedly. **B** Schematic representation of a ring bubble interacting with a vortex fluid, the high-speed camera images show the ring formed around the ring core by the gas following the vortex, providing a visible representation of the vortex structure. **C** Mean circulation (Γ_m) versus output energy, comparing different generation methods, including gravity-driven, piston-driven, and compressed gas-driven. **D** The decay of the vortex-ring-circulation under rebound and jetting, with distinct stages of deflation, oscillation. In the initial stage (0–2 ms), the bubble undergoes rapid expansion and acceleration influenced by the primary bubble's flow field, shock waves, and surrounding fluid. This is followed by deflation and deceleration. After 2 ms (yellow region), the bubble stabilizes and migrates at an approximately

constant velocity for the rebound, including experimental data (solid line) and theoretical attenuation model (dashed line). **E** Oscillatory behavior of the ring bubble radius (R) over time. **F** Oscillatory behavior of the core radius (R_c) over time. **G** Under different constraint tube, the energy increases, the circulation increases, and the state of the vortex ring becomes more stable. **H** It becomes difficult for the electrode to discharge under the slender tube, and part of the energy is converted into arc discharge, which cannot be injected into the vortex ring to increase the circulation. **I** Experimental and theoretical data on the frequency of vortex ring oscillation. As the energy increases, the vortex ring oscillation frequency decreases and the oscillation amplitude increases, which is conducive to running longer distances. Data represented as mean \pm SD in Supplementary Table S3, S4, S5. $^*p < 0.05$. Scale bars, 10 mm. Source data are provided as a Source Data file.

In the piston-driven method, the Kelvin-Benjamin variational principle explains the maximum circulation limit L/D ratio of ~ 4 ⁴¹. The intense energy release produces instantaneous bubble formation and collapse in this method, significantly enhancing vorticity through dynamic instabilities created by fluids with very high velocities and accelerations. This approach surpasses the L/D constraint, enabling the formation of stable vortex rings with higher circulation. Compared with traditional methods, it can give the surrounding fluid a higher speed and acceleration in extremely short time. The generation of the vortex ring in this method is essentially driven by different pulse

energies to generate primary bubbles. Unlike the piston using different L/D to generate different energies directly acting on the vortex ring, the L/D of the container indirectly affects the deformation of the primary bubble, rather than being a direct condition for the dynamic changes of the vortex ring (Fig. 3G)⁴². However, when L is too large and D is extremely small, the water column will suppress the discharge, eventually resulting in arc discharge (Fig. 3H), making it impossible to fully inject energy into the vortex ring.

The oscillation frequency of the vortex ring decreases with the increase of the discharge energy. In the rebound and jetting modes,

the oscillation frequency is about 1000 Hz, which is significantly different from the vortex ring produced by the traditional method (Fig. 3I). This distinction is attributed to the rapid pulse energy injection facilitated by the submerged sparker to give the vortex a larger circulation, and this repetitive oscillation contributes to maintaining the stability of the vortex ring bubble.

Ring bubble translational dynamics

The translational dynamics of ring bubbles generated by a submerged sparker exhibit intricate and highly distinctive characteristics, including elevated velocities, robust circulation, and remarkable stability (Fig. 4A), with different average migration speeds due to different energies and tube shapes (Fig. 4B). The circulation and shape of the vortex ring affect the migration speed. Therefore, as the two oscillate and decay, the speed of the vortex ring gradually decays, which is consistent with the initial Saffman exponential decay and the long-term power function decay (Figs. 4C and 4D)^{40,43}.

In unsteady fluid mechanics, the Kelvin impulse (Eq. 5) describes the effect of buoyancy and the Bjerknes force caused by rough boundary or free surface on the bubble, which affects the direction of the bubble's movement⁴⁴. Figure 4E shows that the motion impulse (Eq. 6) of the high-circulation vortex ring generated by the electric spark is much larger than the Kelvin impulse. Therefore, the movement of the vortex ring is less affected by buoyancy. Compared with the traditional vortex ring that depends on the direction of buoyancy, the vortex ring is less affected by external forces, it can more accurately transport bubbles in a directional manner and can theoretically run for a longer distance. Ultra-long distance transport simulation data is shown in Supplementary Fig. S14.

$$I_x(t) = \frac{\sqrt{6\pi R_m^5} \sqrt{(\Delta p \cdot \rho)}}{9h^2} \left[\pm \frac{2\rho gh^2}{\Delta p \cdot R_m} C_1(t) + BC_2(t) \right] \quad (5)$$

$$M = \rho \pi R^2 \Gamma \quad (6)$$

The exceptional velocity and circulation characteristics of ring bubbles ensure consistent path stability and structural integrity over extended distances (Fig. 4F and Movie S5) with in a transparent tube in Supplementary Fig. S15, and the long tube transportation simulation data is shown in Supplementary Fig. S16. The translational distances varied depending on energy outputs, with rebound mode achieving 400 mm and jetting mode reaching 800 mm within 0.3 to 1 second, respectively (Fig. 4G). Notably, these bubbles did not disintegrate upon reaching 800 mm; the measurement limit was solely due to the bottom boundary of the tube. Figure 4H further illustrates velocity attenuation during long-distance migration stabilizes at ~0.5 m/s (rebound) and 1 m/s (jetting). Interestingly, the direction of migration had minimal influence on bubble dynamics. Unlike traditional buoyancy-driven mechanisms, ring bubbles generated via submerged sparkers exhibited negligible horizontal drift (Fig. 4I), highlighting their superior adaptability for underwater transport across various orientations.

Figures 4J, 4K, 4L shows the different flow field states of the vortex ring with different inputs through the dimensionless constant^{36,45,46} of the vortex ring flow field (Eqs. 7–10). Under different constraint tube, the energy increases, the Reynold number of the vortex ring increases, and the disturbance of the vortex ring to the flow field increases; the Weber number of the vortex ring decreases, and the stability of the movement and shape of the vortex ring is enhanced; the cavitation number of the vortex ring decreases, that is, the vortex ring speed increases, and it is easier to maintain cavitation. As the vortex ring injection energy increases, it is easier to form a vortex ring with a higher circulation and stability. In addition to significantly increasing the circulation, the bubble ring has a small flow field effect, and the

capability of rapidly generating consecutive ring bubbles using pulsed electrical signals has considerable potential for practical applications (Figs. 4M, N and Movie S6). At the same time, Fig. 4O demonstrates that the energy efficiency of vortex rings increases with output energy, whereas the efficiency of primary bubbles peaks at ~3.5% around 3 J^{47,48}.

$$Re = \frac{\Gamma}{\nu} \quad (7)$$

$$\sigma_\nu = \frac{p_0 - p_\nu(T)}{\frac{1}{2}\rho u_m^2} \quad (8)$$

$$We = \frac{R\gamma}{\rho\Gamma^2} \quad (9)$$

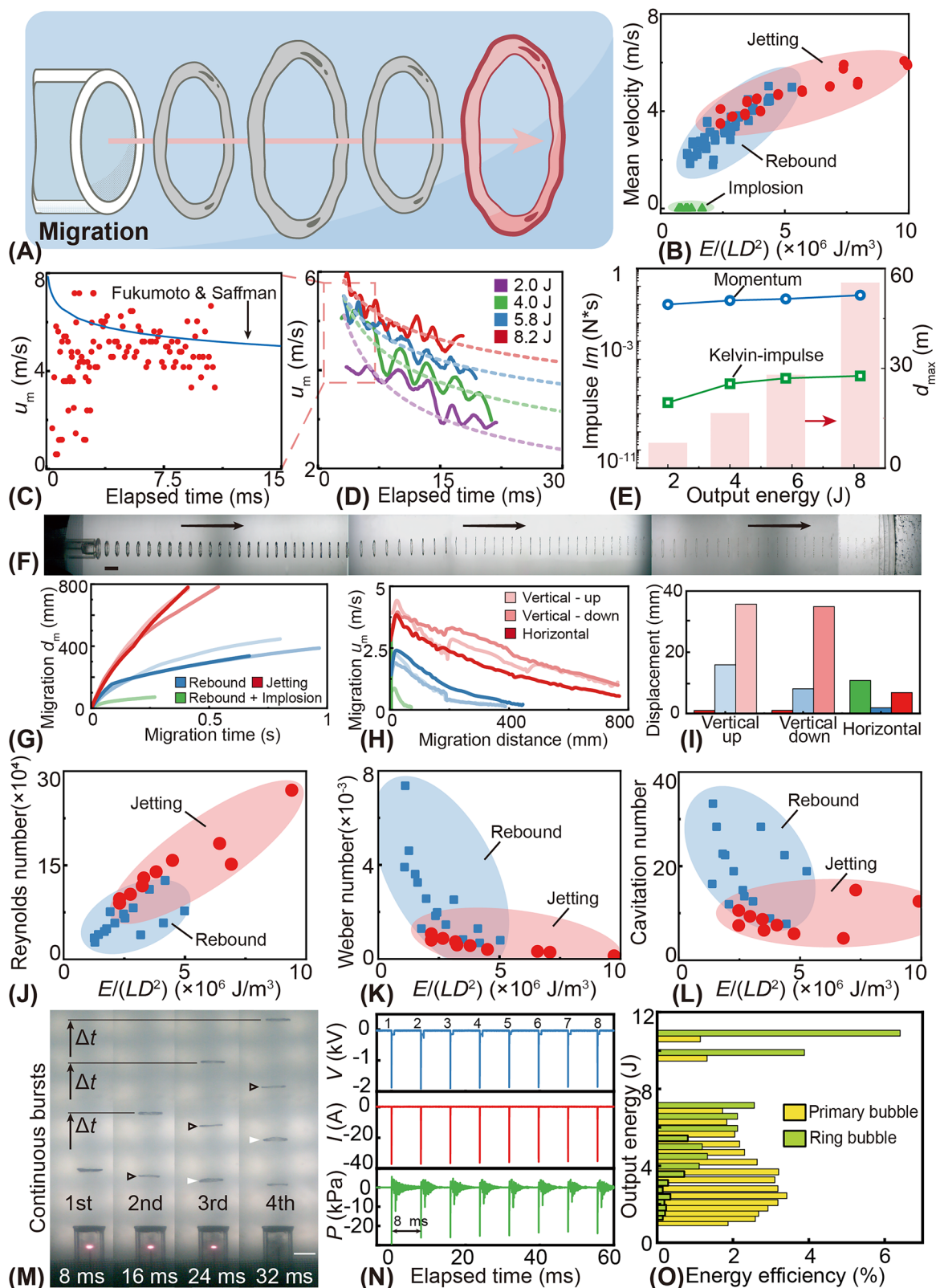
$$Fr = \frac{\Gamma}{\sqrt{2g(\frac{R}{2})^3}} \quad (10)$$

Collapse and collision of ring bubble

Figure 5A shows that when the vortex of the vortex ring decays to the point where it cannot maintain a low cavitation pressure, the vortex ring gas diffusion eventually causes the bubble ring to collapse. After a long period of migration energy decay or collision with a larger range of obstacles (Fig. 5B and Movie S7), such as in narrower tubes, Rayleigh-Taylor instabilities at the interface and wall-induced perturbations amplify asymmetries, causing the ring bubble to eventually shift toward the wall and disintegrate after traveling a certain distance. The high circulation obtained by this method can support its more stable movement over longer distances, and it has strong anti-interference ability against bubble-like obstacles (Supplementary Fig. S17, Movie S8, Movie S9)⁴⁹.

The rapid motion of the ring bubble enables it to preserve its shape and velocity while crossing medium interfaces. As demonstrated in Figs. 5C, 5D and Movie S10, a ring bubble generated in a saline-medium transitions seamlessly across the water-oil interface, maintaining its original velocity and direction in the oil phase (see Supplementary Fig. S18 for supporting data). Unlike a spherical bubble, a rising ring bubble exhibits a pronounced capacity to entrain substantial volumes of the lower liquid through the self-induced circulating flow characteristic of its motion. When the tube opening is positioned at the water-oil interface, the pressure gradient within the tube can be transmitted across phases, directly generating a ring bubble in the oil. Given that submerged sparker operations are more efficient in high-conductivity environments, this cross-medium migration capability is particularly advantageous for applications in low-conductivity conditions. Figure 5E shows through the Froude number that the vortex ring generated by this method has a more stable ability to cross the medium as the energy increases.

Another notable characteristic of the rapid ring bubble lies in its ability to exchange materials during collisions while preserving its original shape and trajectory (Fig. 5F). As illustrated in Fig. 5G, H and Movie S11, Movie S12, two ring bubbles traveling along perpendicular paths undergo mutual distortion along their original planes due to vortex interactions before colliding⁵⁰. At the collision point, both bubbles experience ring breakage at the distorted locations. Subsequently, segments from each of the two original bubbles, now in the same plane, rapidly reconnect to form a new ring bubble, which then propagates in a direction perpendicular to the original planes. The dynamics of this interaction highlight the resilience and adaptability of ring bubbles during complex collisions, including material exchange and structural reformation. Showing in the Flow field parameters of Figs. 5I, 5J, the tearing and reformation of bubble rings during perpendicular collisions is sustained by a sufficiently high velocity by



present method, sufficiently high long-time stable speeds are determined by sufficiently high circulation, ensuring dominance of inertial over viscous and surface tension effects. High-speed rings exhibit better resilience, more stable post-collision structures, and enhanced mixing capabilities. This interesting exchange characteristic is not limited to gas transfer; ring bubbles also exchange entrained materials within vortex thread and bridge (Supplementary Figs. S19, S20).

Magnetic particles are transferred and transported upward by the vertical ring bubble. In both gas and magnetic particle exchange scenarios, the ring diameter of vortex bubbles remains largely unchanged post-collision, while, the restructured ring bubbles exhibit a notable decrease in translational velocity along their original trajectory, ranging from ~30% to 40%. Despite this reduction, as carriers (represented by vertically ascending vortex bubbles in this experiment), they

Fig. 4 | Ring bubble translational dynamics. **A** During the movement of ring, due to the oscillation and decay of the circulation and radius, its speed also oscillates and decays. **B** Under different tube, energy increases, speed increases. **C** Comparison between experimental ring bubble velocity and theoretical predictions by Fukumoto and Saffman. While early equilibrium velocities align well with predictions, deviations occur in initial velocity estimates due to temporal and spatial resolution limitations. The model consistently overestimates long-distance velocities due to inadequate dissipation of circulation. **D** The velocity and decay model of the vortex ring in a long period of time, the decay is fast in early stage and relatively stable in later stage. **E** The impulse of ring at different energies and the theoretical maximum travel distance. **F** Overlay of high-speed camera images showing the trajectory of a ring bubble migrating horizontally within a long transparent tube (details in Supplementary

Fig. S15). **G** Translational distances (d_m) of ring bubbles at different energy outputs for three states. **H** Migration velocity (u_m) of ring bubbles as a function of migration distance, illustrating velocity attenuation over time for different migration directions. **I** Displacement of ring bubbles under varying migration directions, indicating minimal horizontal drift compared to vertical migration. **J** Under different tube, energy increases, the Reynold number of vortex ring increases. **K** The Weber number. **L** The cavitation number. **M** Sequential generation of multiple ring bubbles at 8 ms intervals ($E_{out} = 5.2$ J). **N** The voltage (V), current (I), and sound pressure (P) signals for multiple ring generation. the uniform spacing between multiple peaks indicates excellent repeatability in pulsed generation. **O** Energy efficiency of bubbles, the energy efficiencies of ring bubble are the ratio between ring and primary bubble. Scale bars, 10 mm. Source data are provided as a Source Data file.

maintain a transport efficiency of ~110%–200%, while the residual content within the transverse bubbles is ~30%–40% (refer to Supplementary Fig. S21). The ability of ring bubbles to undergo collision-induced topological changes and continue propagation could be leveraged in multiple areas, such as propulsion and gas-liquid reactors.

Submerged-sparker ring bubbles scale from 30 mm down to 1.7 mm via different constraint tubes (Supplementary Fig. S22 and Movie S13), which is beyond the limits of the mechanical system of the piston system. Driven by localized energy rather than bulk gas injection, they contain minimal gas and offer superior control versus compressed-air bubbles, enabling ultra-small rings for precise fluid handling, targeted drug delivery, or microscale diagnostics with high accuracy and low invasiveness.

Utilizing the features of the rapid ring bubble

This vortex flow demonstrates significant potential for the stable transport of substantial quantities of entrained materials³¹. In this study, magnetic particles (Fe_3O_4 , mean diameter $D_m = 45 \mu\text{m}$), glass microspheres (SiO_2 , $D_m = 800 \mu\text{m}$), and micro gas bubbles (Air, $D_m = 1000 \mu\text{m}$) are selected as transport targets. As shown in Fig. 6A, all three materials underwent continuous rotation around the ring bubble, enabling their transport along the bubble's trajectory.

Magnetic particles at the tube opening are rapidly entrained by the ring bubble, wrapping tightly around the vortex core with angular velocity peaking inward Supplementary Fig. S13), causing energy dissipation, dispersion, a visible sheath and a trailing stream (Supplementary Figs. S21, S23; and Movie S14, S15). Glass microspheres behave similarly but detach more readily due to higher inertia, though gas-interface merging shifts their transport to direct integration; microbubbles are drawn inward—stretching, deforming, or fragmenting—before merging with the core (Movie S16). In the transportation and recycling experiments (Fig. 6B) of three materials, Fig. 6C confirms smaller, denser particles couple most strongly, yielding higher rotational speeds; magnetic particles recover at 30%–47% (Fig. 6D, red), glass microspheres travel ~30–40 mm (Fig. 6D, blue), and post-air-curtain ring thickening via rapid gas interface merging achieves 72%–91% transport efficiency (Fig. 6D, purple). Building on these findings, a ring bubble relay transport experiment is conducted (Supplementary Fig. S24 and Movie S17). The ring bubbles rely on high circulation to maintain stability of transport despite directional changes and interactions with subsequent discharge phases.

The translational distance and migration velocity of submerged discharge-induced ring bubbles are compared with several other directional bubble transport methods (data in Supplementary Data S1). A ring bubble generated by a submerged sparker can migrate over 800 mm (Fig. 6E) and achieve velocities exceeding 8000 mm/s with an initial velocity up to 12000 mm/s (Fig. 6F), comparable to other bubble transport mechanisms. Compared to existing bubble transport methods driven by buoyancy, Laplace pressure differentials, or external forces, the submerged sparker-induced ring bubble demonstrated superior performance in terms of translational distance, migration velocity, stability, repeatability, controllability, robustness, ease of fabrication, and

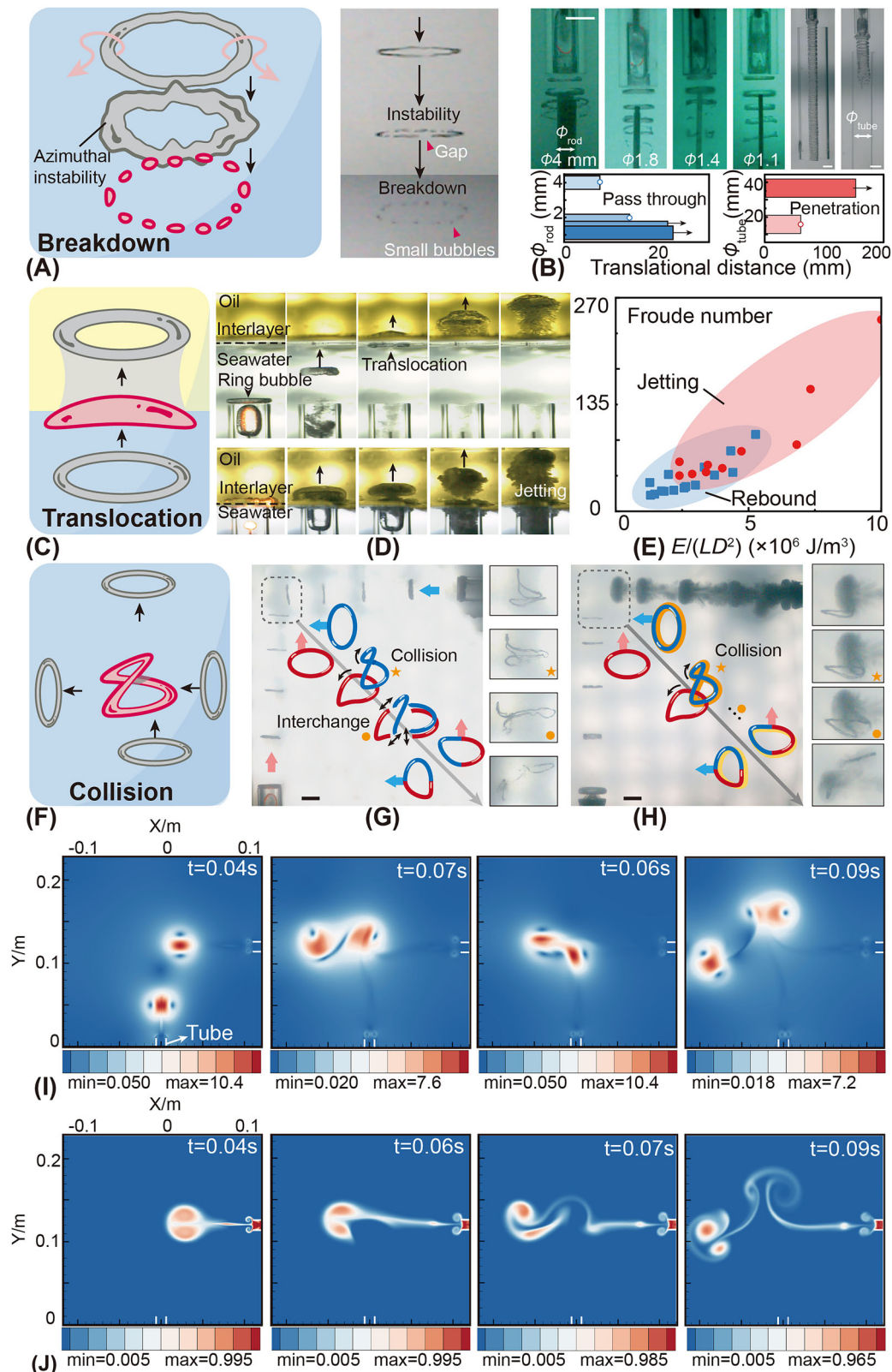
cost-effectiveness. Due to limited comparable data, Fig. 6G presents the gas transport capabilities of various methods in terms of maximum gas transport volume. The proposed method's maximum gas transport volume (~2100 μL) significantly surpassed that of other methods. Despite the high transport capacity, the volume of the ring bubble itself remained small (0.1–0.2 μL), minimizing interference with the transported gas and avoiding significant accumulation or mixing.

In addition, we observed that vortex ring can produce significant impact when it hits the wall. The vibration acceleration generated by the high-speed vortex ring impacting at different positions on the 40.9 cm \times 29.7 cm \times 45.8 cm wall was measured in Supplementary Fig. S25, S26, and S27. The impact effect related to the bubble ring velocity was observed at the impact position, indicating that the high-speed vortex ring has the potential to study bubble explosion dynamics, pipeline wall cleaning, etc.

Compared to other methods for generating ring bubbles, such as gravity-driven, piston-driven, and compressed air-driven systems (Supplementary Fig. S28 and Supplementary Data S2), the proposed method achieved a maximum circulation number of 8000 cm^2/s , which was considerably higher than other methods. This increased circulation enhanced the velocity, stability, and transport capacity of the ring bubble. The submerged sparker system (Supplementary Fig. S29) also demonstrated superior adaptability, accommodating a minimum ring diameter of 1.7 mm and expandable maximum diameters of up to 30 mm (as achieved in this study), the nozzle or orifice used had a minimum diameter as small as 1 mm, surpassing the flexibility of widely used piston-driven or compressed air-driven systems. Furthermore, pulsed discharge energization allowed for the high-frequency, continuous generation of ring bubbles within a single system, eliminating the need for nozzle arrays or multiple high-pressure switches, thereby significantly enhancing its applicability.

Discussion

This study introduces an advanced technique for generating and manipulating ring bubbles via submerged spark discharge, demonstrating clear performance gains over piston and compressed-gas methods. The rapid energy transfer from the spark drives the fluid to much higher velocities and accelerations in milliseconds, producing vortex rings with substantially greater circulation. The high initial pressure and rapid expansion of the primary bubble create a concentrated vorticity layer at the tube's exit, facilitating the formation of a stable, high-speed ring bubble without direct dependence on the L/D . This contrasts sharply to piston-driven methods which has L/D limitations, highlighting the efficiency of the sparker approach. The generated ring bubbles exhibit exceptional mobility, translating horizontally over distances up to 800 mm with minimal center drift. Furthermore, their robust circulation allows for efficient entrainment and transport of particles and microbubbles, demonstrating potential in microfluidics, drug delivery, and other applications. The scalability of the method, demonstrated by generating ring bubbles from macroscopic down to 1.7 mm in diameter, further broadens its potential impact. The ring bubbles' resilience against perturbations and their ability to



traverse obstacles and cross interfaces underscores their robustness and opens up new possibilities for complex, controlled manipulations in fluid environments. The high repetition rate achieved with pulsed energization adds another layer of control, allowing for rapid, sequential generation of ring bubbles for applications requiring high throughput or dynamic manipulation. The 8 J-level vortex ring generated by this method can bring an impact acceleration of up to 45 m/s^2

at a distance of 29 cm. The impact vibration it generates can effectively peel off and shake off pollutants attached to complex walls through small-range, high-amplitude, controllable-frequency pressure pulses and structural vibrations without contacting the wall. It can also be used to study the dynamics of submerge bubble explosions.

While this study demonstrates the capabilities of submerged sparker-generated ring bubbles, certain limitations require further

Fig. 5 | Collapse and collision of ring bubble. **A** As the vortex ring speed and flow field speed slow down, the ring bubble gas diffuses into small bubbles. Right picture shows the collapse process captured by high-speed camera. **B** High-speed images showing the ring bubble passing through rods of varying diameters (ϕ_{rod}) and tubes (ϕ_{tube}). Translational distance indicates the threshold for penetration and successful traversal of obstacles. Hollow circles indicate bubble decay at specific position and arrows represent rings maintain the shape after traversing specific position. **C** The ring can maintain the motion stability when passing through the two-phase medium and carry the substances in the previous phase. **D** Sequential images of a ring bubble generated in saline medium crossing the water-oil interface. Above subfigure shows the ring translocating through the interface and maintains its integrity, bottom subfigure shows ring bubble generated at the water-oil interface and migrate in the oil. **E** Under different constraint tube, energy increases, the

Froude number of vortex ring increases, its material carrying capacity and stability across the medium becomes stronger. **F** In collision of two rings, three key stages can be divided into the first reconnection, the bridge/thread, and the second reconnection. Substances can be exchanged via bridge, ultimately achieving converting the direction of transported substances. **G** Interaction of two rings traveling along perpendicular paths. **H** Exchange of magnetic particles between two colliding ring bubbles. The magnetic particles carried by the horizontally migrating ring bubble are partially transferred to the vertically migrating ring bubble upon collision. **I** Velocity (m/s) distribution of vortex rings merging and separating during collision. **J** Material composition of vortex ring merging and separation during collision. The surrounding component of the vortex ring is carried away by another vortex through bridge. Scale bars, 10 mm. Source data are provided as a Source Data file.

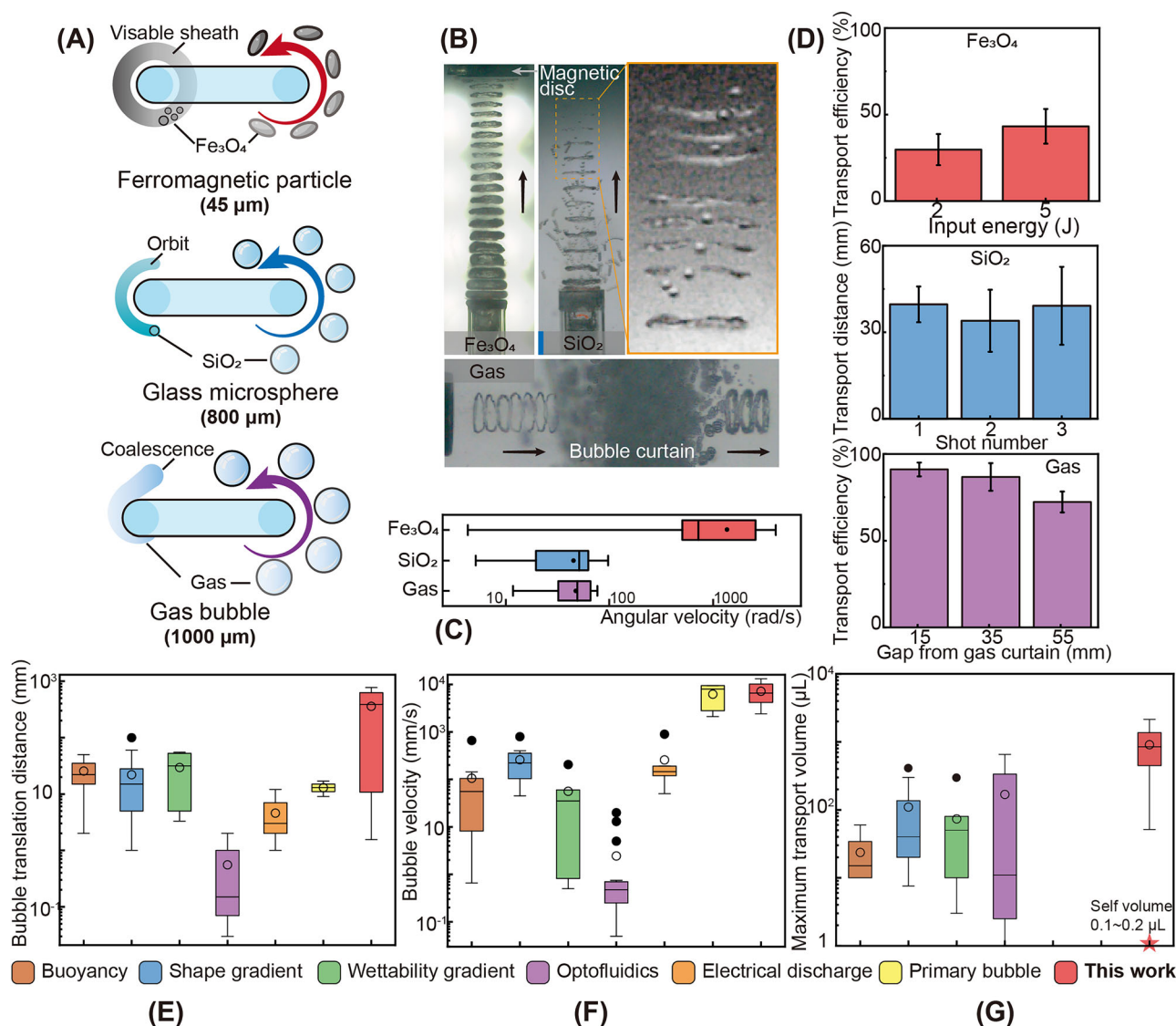


Fig. 6 | Transport mechanism and efficiency of ring bubbles carrying different particles. **A** Schematic representation of the transport mechanism for different types of particles: magnetic particles (Fe_3O_4 , $45\ \mu\text{m}$), glass microspheres (SiO_2 , $800\ \mu\text{m}$), and gas bubbles ($1000\ \mu\text{m}$). **B** Complete transport process for magnetic particles, glass microspheres, and gas bubbles. The ring bubbles generated via submerged sparker exhibit high circulation, with the surrounding rotational vortex steadily entraining adjacent fluid layers for long periods of time. **C** Angular velocity of different particle types around the ring core, with the horizontal axis presented on a logarithmic scale. Magnetic particles achieved the highest speed, reaching up

to 1000 rad/s, while glass microspheres and gas bubbles rotate at 10–100 rad/s. **D** Transport performances for three particle types. **E** Comparison of bubble translational distances among different transport methods. **F** Comparison of bubble velocity for various bubble transport mechanisms. **G** Maximum transport volume achieved by the proposed submerged sparker system compared to other bubble generation methods. Due to the significant variation in data, the vertical axes of Fig. 6 E to G are presented on a logarithmic scale. Reference is list in Supplementary Data S1. Data represented as mean \pm SD. * $p < 0.05$ in. Scale bars, 10 mm. Source data are provided as a Source Data file.

investigation. A more refined model incorporating factors like boundary effects and turbulence is needed for improved predictive accuracy. Additionally, more detailed analysis of the energy transfer mechanisms during the discharge process, including the interplay between shock wave dynamics, cavitation, and vorticity generation, would provide valuable insights for optimizing the system's efficiency and controllability. Studying the interaction of multiple ring bubbles in different configurations could lead to innovative strategies for manipulation and transport in microfluidic devices or other fluidic systems.

Methods

Submerged spark discharge

The submerged spark discharge method leverages state-of-the-art solid-state pulsed power technology to generate high-energy plasma discharges within aqueous environments. The system architecture is based on a three-stage AC/DC pulse converter that charges a high-voltage capacitor to ~ 5 kV within ~ 200 ms, enabling energy pulses in the range of 0 to 90 J at repetition rates between 0.5 and 2 pulses per second (pps). The capacitor discharge is regulated by a high-performance thyristor switch, delivering energy outputs up to 90 J per pulse, with peak currents reaching 1.3 kA and pulse durations spanning 80–200 μ s. To accommodate elevated current demands, the design incorporates an innovative circuit topology employing multiple synchronized switches. This approach effectively sustains high-power submerged spark discharge plasmas with enhanced reliability. The circuits are meticulously engineered to support pulse durations in the microsecond to nanosecond range, as rapid discharge times are pivotal for achieving efficient bubble generation. Prolonged discharge intervals would result in increased energy dissipation as heat, thereby diminishing the energy available for vaporization and bubble expansion. By confining energy deposition to the spark gap within extremely brief timeframes, the system ensures rapid localized heating and immediate vaporization of the surrounding water, leading to the formation of a vapor primary bubble prior to substantial heat diffusion.

Multiple channel energization

The eight-channel energization circuit integrates input and charging stages with eight parallel discharge branches, each independently configured with dedicated energy storage, switching components, and inductors. Sharing a common high-voltage DC source, these branches enable selective triggering for high-current, short-duration pulses, driving submerged electrodes to generate bubbles. This structure allows simultaneous or sequential activation of channels for enhanced functionality.

Vortex ring generation

Conventional submerged discharge uses a 3.5% saline solution to complete the circuit. Here, a quartz tube ($D=10$ mm) surrounds the electrode as a rigid boundary, set 12 mm from its rim ($L/D=1.2$, well below the 3.6–4.5 piston threshold), to facilitate boundary-layer separation. In piston systems, vorticity is generated by boundary layer separation at the nozzle edge and its subsequent roll-up, with stroke length L dictating circulation and requiring long strokes for pinch-off. In our sparker method, the primary bubble's rapid expansion sends a radial shock wave against the tube walls. The bubble's high pressure supplies ample impulse and circulation for rapid pinch-off, despite low L/D and minimal water displacement.

Statistical analysis

The number of experimental repetitions for each group with different energies and different cannulas was $n \geq 3$, and all data were analyzed. The experimental data were expressed as mean \pm SEM due to small errors. The t-test was used for analysis between two groups with one variable. Statistical significance was set at $*p \leq 0.05$.

Data availability

Source data are provided with this paper. Any additional requests for information can be directed to the corresponding author. Source data are provided with this paper.

Code availability

The code that supports the findings of this study are available from the corresponding author upon request. No custom code was used in this study. All analyses were performed using standard MATLAB functions.

References

- Janiak, J. et al. Acoustic microbubble propulsion, train-like assembly and cargo transport. *Nat. Commun.* **14**, 4705 (2023).
- Han, K. & Yong, K. Overcoming limitations in surface geometry-driven bubble transport: bidirectional and unrestricted movement of an underwater gas bubble using a magnetocontrollable non-wetting surface. *Adv. Funct. Mater.* **31**, 2101970 (2021).
- Yan, X. et al. Bubble energy generator. *Sci. Adv.* **8**, eabo7698 (2022).
- Li, X. et al. Bubble up induced graphene microspheres for engineering capacitive energy storage. *Adv. Energy Mater.* **13**, 2203761 (2023).
- Jia, M. et al. Nanobubbles in water and wastewater treatment systems: Small bubbles making big difference. *Water Res.* **245**, 120613 (2023).
- Kim, Y. J. et al. Highly efficient oxygen evolution reaction via facile bubble transport realized by three-dimensionally stack-printed catalysts. *Nat. Commun.* **11**, 4921 (2020).
- Zhu, S. et al. High performance bubble manipulation on ferrofluid-infused laser-ablated microstructured surfaces. *Nano Lett.* **20**, 5513–5521 (2020).
- Orvalho, S., Stanovsky, P. & Ruzicka, M. C. Bubble coalescence in electrolytes: Effect of bubble approach velocity. *Chem. Eng. J.* **406**, 125926 (2021).
- Hu, M. et al. Near-infrared-laser-navigated dancing bubble within water via a thermally conductive interface. *Nat. Commun.* **13**, 5749 (2022).
- Chen, S. et al. Collective buoyancy-driven dynamics in swarming enzymatic nanomotors. *Nat. Commun.* **15**, 9315 (2024).
- Xiao, X. et al. Bioinspired two-dimensional structure with asymmetric wettability barriers for unidirectional and long-distance gas bubble delivery underwater. *Nano Lett.* **21**, 2117–2123 (2021).
- Tiribocchi, A. et al. The vortex-driven dynamics of droplets within droplets. *Nat. Commun.* **12**, 82 (2021).
- Wadas, M. J. et al. Saturation of vortex rings ejected from shock-accelerated interfaces. *PRL* **130**, 194001 (2023).
- Pedrizetti, G. et al. The vortex—an early predictor of cardiovascular outcome?. *Nat. Rev. Cardiol.* **11**, 545–553 (2014).
- Moon, E., Song, M. & Kim, D. Liquid entrainment of the toroidal bubble crossing the interface between two immiscible liquids. *J. Fluid Mech.* **966**, A27 (2023).
- Dabiri, J. O. & Gharib, M. Fluid entrainment by isolated vortex rings. *J. Fluid Mech.* **511**, 311–331 (2004).
- Xiang, Y., Qin, S. & Liu, H. Patterns for efficient propulsion during the energy evolution of vortex rings. *Eur. J. Mech. B Fluids* **71**, 47–58 (2018).
- Zhu, J. et al. Vortex ring formation process in starting jets with uniform background co- and counter-flow. *J. Fluid Mech.* **968**, A26 (2023).
- Gharib, M., Rambod, E. & Shariff, K. A universal time scale for vortex ring formation. *J. Fluid Mech.* **360**, 121–140 (1998).
- Zhang, L. et al. Thermodynamic characteristics of the hot-temperature cavity generated by the spark discharge in saline water. *Int. J. Heat Mass Transf.* **215**, 124498 (2023).
- Ji, B., Yang, Z. & Feng, J. Compound jetting from bubble bursting at an air-oil-water interface. *Nat. Commun.* **12**, 6305 (2021).

22. Zhang, L. et al. Influence of discharge polarity on the dynamics of spark-induced bubble in saline water. *Appl. Phys. Lett.* **123**, 054101 (2023).
23. Huang, Y. et al. Experimental observation of the luminescence flash at the collapse phase of a bubble produced by pulsed discharge in water. *Appl. Phys. Lett.* **107**, 184104 (2015).
24. Ji, C., Lin, F.-Y. & Zou, J. Experimental investigation of vortex-ring cavitation. *J. Zhejiang Univ. Sci.* **18**, 545–552 (2017).
25. Xu, M. et al. Particle removal by a single cavitation bubble. *Sci. China: Phys. Mech. Astron.* **57**, 668–673 (2014).
26. Pavard, D. et al. Removal of particles from holes in submerged plates with oscillating bubbles. *Phys. Fluids*. **21**, 083304 (2009).
27. Lew, K. S. F., Klaseboer, E. & Khoo, B. C. A collapsing bubble-induced micropump: An experimental study. *Sens. Actuators A: Phys.* **133**, 161–172 (2007).
28. Oshita, D. et al. Two Successive Shock Waves Generated by Underwater Pulse Electric Discharge for Medical Applications. *IEEE Trans. Plasma Sci.* **42**, 3209–3214 (2014).
29. Reader, J. et al. Wavelengths and transition probabilities for atoms and atomic ions::part I. wavelengths - part II. transition probabilities. *National Institute of Standards and Technology*, (1980).
30. Kepple, P. & Griem, H. R. Improved Stark profile calculations for the hydrogen lines H_{α} , H_{β} , H_{γ} , and H_{δ} . *Phys. Rev.* **173**, 317 (1968).
31. Namihiro, T. et al. Electron temperature and electron density of underwater pulsed discharge plasma produced by solid-state pulsed-power generator. *IEEE Trans. Plasma Sci.* **35**, 614–618 (2007).
32. Lukes, P. et al. Erosion of needle electrodes in pulsed corona discharge in water. *Czech. J. Phys.* **56**, B916–B924 (2006).
33. Goryachev, V. L., Ufimtsev, A. A. & Khodakovskii, A. M. Mechanism of electrode erosion in pulsed discharges in water with a pulse energy of similar to 1 J. *Tech. Phys. Lett.* **23**, 386–387 (1997).
34. Jiao, Z. et al. Dynamics of spark cavitation bubbles in a micro-chamber. *Microfluid. Nanofluid.* **25**, 19 (2021).
35. Tinguely, M. The effect of pressure gradient on the collapse of cavitation bubbles in normal and reduced gravity. *EPFL*, 5674 (2013).
36. Franc, J.-P. & Michel, J.-M. *Fundamentals of cavitation*. Springer science & Business media (2006).
37. Marten, K. et al. Ring bubbles of dolphins. *Sci. Am.* **275**, 82–87 (1996).
38. Biswas, S. & Govardhan, R. N. Vortex ring and bubble interaction: Effects of bubble size on vorticity dynamics and bubble dynamics. *Phys. Fluids*. **35**, 083328 (2023).
39. Saffman, P. G. Velocity of viscous vortex rings. *Stud. Appl. Math.* **49**, 371 (1970).
40. Dziedzic, M. & Leutheusser, H. J. An experimental study of viscous vortex rings. *Exp. Fluids* **21**, 315–324 (1996).
41. Limbourg, R. & Nedić, J. Formation of an orifice-generated vortex ring. *J. Fluid Mech.* **913**, A29 (2021).
42. Gong, S. W. et al. Scaling law for bubbles induced by different external sources: Theoretical and experimental study. *Phys. Rev. E*. **81**, 056317 (2010).
43. Fukumoto, Y. & Moffatt, H. K. Kinematic variational principle for motion of vortex rings. *Phys. D*. **237**, 2210–2217 (2008).
44. Lamb, H. *Hydrodynamics*. Cambridge University Press (1924).
45. Xu, Y. H. et al. Instability of a swirling bubble ring. *C. R. Mec.* **348**, 519–535 (2020).
46. Wu, C. J., Fu, Q. & Ma, H. Y. Interactions of 3-dimensional viscous axisymmetrical vortex rings with a free-surface. *Acta Mech. Sin.* **11**, 229–238 (1995).
47. Wen, H. G. et al. Energy partitioning in laser-induced millimeter-sized spherical cavitation up to the fourth oscillation. *Ultrason. Sonochem.* **95**, 106391 (2023).
48. Jha, N. K. & Govardhan, R. N. Interaction of a vortex ring with a single bubble: bubble and vorticity dynamics. *J. Fluid Mech.* **773**, 460–497 (2015).
49. New, T. H., Xu, B. & Shi, S. Collisions of vortex rings with hemispheres. *J. Fluid Mech.* **980**, A17 (2024).
50. Kida, S., Takaoka, M. & Hussain, F. Collision of 2 vortex rings. *J. Fluid Mech.* **230**, 583–646 (1991).
51. Li, L. et al. Fluid-induced transport dynamics and vibration patterns of multiphase vortex in the critical transition states. *Int. J. Mech. Sci.* **252**, 108376 (2023).

Acknowledgements

The authors gratefully acknowledge Prof. Yifan Huang, Dr. Hui Yan, and Prof. Liancheng Zhang for their foundational research work that laid the groundwork for this study. We also thank Dr. Hong Cao for his generous contributions to the simulation work involved in this research. Funding: This work was partially supported by grants from: National Key R&D Program of China grant 2023YFC2811201 (S.L.), and Major Research Project on Scientific Instrument Development, National Natural Science Foundation of China grant 42327901 (S.L.).

Author contributions

Conceptualization: X.W., Y.F., and S.L. Methodology: X.W., Y.F., and S.L. Investigation: X.W., Y.F., S.L., and S.Z. Visualization: X.W., Y.F., and S.L. Supervision: S.L., H.C., S.Z., Z.L., Y.P., W.Z., X.S., Y.K., and K.Y. Writing—original draft: X.W., Y.F., S.L., and S.Z. Writing—review & editing: X.W., Y.F., S.L., and S.Z.

Competing interests

Authors declare that they have no competing interests.

Additional information

Supplementary information The online version contains supplementary material available at <https://doi.org/10.1038/s41467-025-61569-5>.

Correspondence and requests for materials should be addressed to Shuran Li.

Peer review information *Nature Communications* thanks the anonymous reviewers for their contribution to the peer review of this work. A peer review file is available.

Reprints and permissions information is available at <http://www.nature.com/reprints>

Publisher's note Springer Nature remains neutral with regard to jurisdictional claims in published maps and institutional affiliations.

Open Access This article is licensed under a Creative Commons Attribution-NonCommercial-NoDerivatives 4.0 International License, which permits any non-commercial use, sharing, distribution and reproduction in any medium or format, as long as you give appropriate credit to the original author(s) and the source, provide a link to the Creative Commons licence, and indicate if you modified the licensed material. You do not have permission under this licence to share adapted material derived from this article or parts of it. The images or other third party material in this article are included in the article's Creative Commons licence, unless indicated otherwise in a credit line to the material. If material is not included in the article's Creative Commons licence and your intended use is not permitted by statutory regulation or exceeds the permitted use, you will need to obtain permission directly from the copyright holder. To view a copy of this licence, visit <http://creativecommons.org/licenses/by-nc-nd/4.0/>.

© The Author(s) 2025